Inorganic Chemistry

Article

pubs.acs.org/IC

Reduced Graphene Oxide-Induced Recrystallization of NiS Nanorods to Nanosheets and the Improved Na-Storage Properties

Qin Pan,[†,‡] Jian Xie,*[,†,‡] Tiejun Zhu,[†] Gaoshao Cao,[‡] Xinbing Zhao,*[,†,‡] and Shichao Zhang[§]

[†]Department of Materials Science and Engineering, State Key Laboratory of Silicon Materials, Zhejiang University, Hangzhou 310027, P.R. China

[‡]Key Laboratory of Advanced Materials and Applications for Batteries of Zhejiang Province, P.R. China

[§]School of Materials Science and Engineering, Beijing University of Aeronautics and Astronautics, Beijing 100191, P.R. China

Supporting Information

ABSTRACT: Preparation of two-dimensional (2D) graphene-like materials is currently an emerging field in materials science since the discovery of single-atom-thick graphene prepared by mechanical cleavage. In this work, we proposed a new method to prepare 2D NiS, where reduced graphene oxide (rGO) was found to induce the recrystallization of NiS from nanorods to nanosheets in a hydrothermal process. The process and mechanism of recrystallization have been clarified by various characterization techniques, including scanning electron microscopy (SEM), transmission electron microscopy (TEM), energy dispersive X-ray spectroscopy (EDS) mapping, and X-ray photoelectron spectroscopy (XPS). The characterization of ex situ NiS/rGO products by SEM and EDS mapping indicates that the recrystallization of NiS from nanorods to nanosheets is realized actually through an exfoliation process, while the characterization of in situ NiS/rGO products by SEM, TEM, and EDS mapping reveals the exfoliation process. The XPS result demonstrates that hydrothermally assisted chemical bonding occurs between NiS and rGO, which induces the exfoliation of NiS nanorods into nanosheets. The obtained NiS/rGO composite shows promising Na-storage properties.

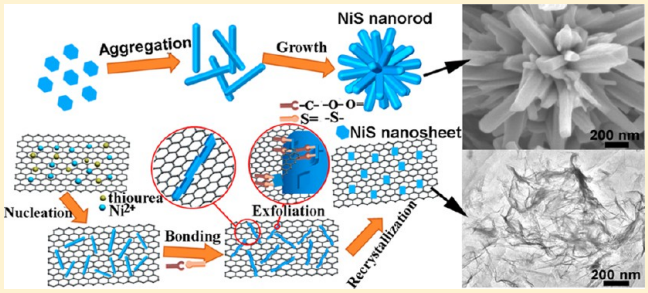

INTRODUCTION

Graphene, a typical two-dimensional (2D) material, has aroused intensive research topics since the pioneering work by Novoselov et al.,[1] due to its unique properties, including large specific surface area,[2] high electrical conductivity,[3] giant mobility of charge carriers[4] and huge mechanical strength.[5] These novel properties make graphene and graphene-based materials promising applications in various fields, such as transistors, sensors, energy storage and conversion, photocatalysis, etc.[6−14] Inspired by the advances in graphene research, an increasing interest has been focused on graphene-like 2D materials with some unusual properties.[15,16] Typically, these 2D graphene analogues were made from layered materials, such as boron nitride and transition metal dichalcogenides (MoS_2, WS_2, WSe_2, etc.), with potential applications in transistors,[17,18] sensors[19,20] and CO_2 absorbent.[21] 2D MoS_2[22] and WS_2[23] also showed promising applications in Li-ion batteries for short Li-ion diffusion pathways and large exposed surface to electrolytes.[24]

Diverse approaches such as mechanical exfoliation,[17,18] liquid exfoliation,[25,26] chemical[21] and electrochemical[19] lithiation, and chemical vapor deposition,[27] have been proposed to prepare 2D graphene-like materials. However, these methods generally involve a complex process with low yield, which are not practical for large-scale production. In addition, for nonlayered materials, it is difficult to obtain graphene-like structure via a facile route unless a complex process is introduced, for example, using organic ligand molecules.[28,29] In this work, graphene-like NiS was prepared by a new exfoliation method, in which reduced graphene oxide (rGO) was used as the "adhesive tape" to "pull" NiS nanosheets out of NiS nanorods. This method is inspired by Novoselov' work of preparing monolayer graphene by mechanical cleavage of graphite using "Scotch tape method",[1] which was extended to prepare other 2D inorganic crystals.[30]

Graphite oxide (GO) can dissolve in water and some polar solvents[31] due to the presence of abundant oxygen-containing groups including epoxy, hydroxyl, carbonyl, and carboxyl groups.[32,33] Although bulk GO also shows a stacked structure similar to graphite, it can be easily dispersed in water (or some polar solvents) to form monolayer or few-layer graphene oxide sheets because of its hydrophilic nature by forming hydrogen bonds between oxygen-containing groups and water molecules.[32,34] The presence of the oxygen-containing groups also makes it possible to functionalize graphene oxide (or rGO) with various organic molecules in solution through covalent and noncovalent approaches.[35−37] In addition, strong coupling between inorganic particles and graphene oxide (or rGO) could also be established through possible chemical bonding.[38,39] In

Received: November 28, 2013
Published: March 19, 2014

   dx.doi.org/10.1021/ic402948s | Inorg. Chem. 2014, 53, 3511−3518

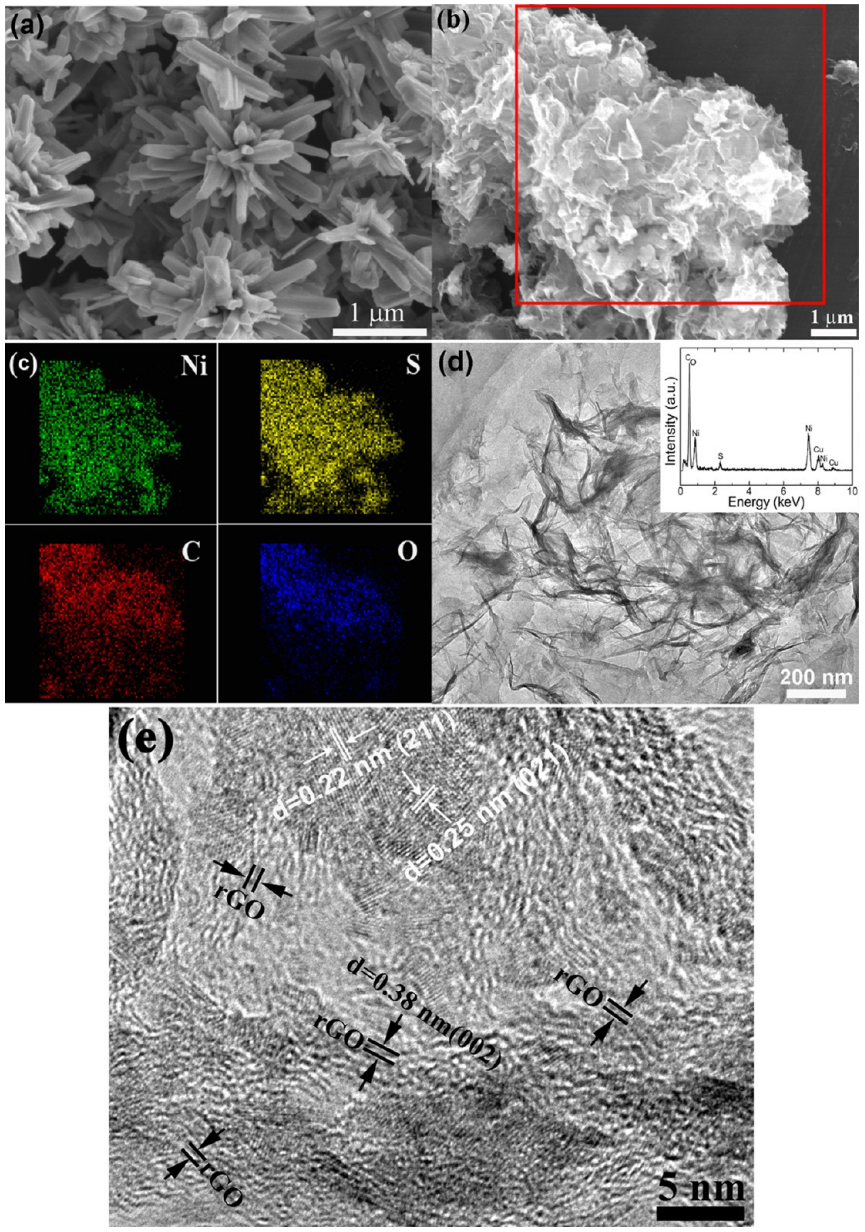

Figure 1. SEM images of (a) bare NiS and (b) NiS/20rGO, (c) EDS mapping of the marked domain in (b), and (d) TEM and (e) HRTEM images of NiS/20rGO.

all the above cases, the strong interaction could be realized through chemical bonding.

In this work, we found that chemical bonding also occurs between the oxygen-containing groups on rGO sheets and the surface chemical bonds on NiS nanorods, which induces the exfoliation of NiS nanorods into nanosheets by weakening the binding force between surface NiS layers and bulk NiS rods. This process can be considered as recrystallization of NiS from nanorods to nanosheets since both are in crystalline state. The exfoliation process and mechanism were revealed by the systematic characterization of a series of ex situ and in situ hydrothermal products with the use of scanning electron microscopy (SEM), transmission electron microscopy (TEM), energy dispersive X-ray spectroscopy (EDS) mapping, and X-ray photoelectron spectroscopy (XPS).

This work provides a new method to prepare graphene-like crystals or hybrids which show appealing applications in various fields. As a potential application in Na-ion batteries, the electrochemical Na-storage properties of NiS/G composite have been studied in this work. Na-ion batteries have long been considered as alternatives to Li-ion batteries because of the natural abundance of Na sources.[40−42] The results show that the NiS/rGO composite exhibits better Na-storage properties than the NiS nanorods due to its unique sheetlike structure. The NiS/rGO composite can yield an initial charge capacity of 181 mA h g^{-1} at a charge current of 200 mA g^{-1}, much higher than that of graphite.[43]

■ EXPERIMENTAL SECTION

In Situ Synthesis of NiS/rGO Composites. For the in situ synthesis of NiS/rGO, a certain amount of GO (10, 20, 30, and 40 mg), prepared by a modified Hummer's method,[44] was added to 50 mL deionized (DI) water with vigorous sonication for 0.5 h to form dispersions with different GO concentrations. Then 1 mmol $Ni(Ac)_2 \cdot 4H_2O$, 3 mmol thiourea, and 1 mmol $Na_3C_6H_5O_7 \cdot 2H_2O$ were added

dx.doi.org/10.1021/ic402948s | Inorg. Chem. 2014, 53, 3511−3518

to each of the above dispersions with stirring. The pH was adjusted to 12 by dropwise addition of 2 mL ammonia solution (28 wt %). After being stirred for another 1 h, the mixed solution was transferred to a Teflon-lined stainless steel autoclave (100 mL in capacity) and heated in an electric oven at 180 °C for 24 h. Finally, the autoclave was cooled down to room temperature naturally. The resultant black precipitates were collected by centrifugation, washed repeatedly with DI water and anhydrous ethanol, and dried at 40 °C under vacuum overnight. According to the carbon content analysis, the rGO contents are around 5, 10, 15, 20 wt % in four NiS/rGO samples, which are named NiS/5rGO, NiS/10rGO, NiS/15rGO and NiS/20rGO, respectively.

Synthesis of Control Samples. For NiS/20rGO, another three samples were also synthesized by performing the hydrothermal reactions for 3, 6, and 12 h while keeping the other conditions unchanged. Bare NiS was also prepared with a similar route (180 °C, 24 h) except for the absence of GO in the precursor. Bare rGO was prepared by the hydrothermal method at 180 °C for 24 h (or 1 h) using GO as the precursor. An ex situ hydrothermal route (180 °C, 24 h) was also used to prepare two NiS/rGO composites (20 wt % rGO) using pre-prepared NiS nanorods and rGO (or GO) as the precursors. The two ex situ prepared NiS/rGO samples are named NiS@20rGO-1 and NiS@20rGO-2.

Materials Characterization. The crystalline phases of the products were identified by XRD on a Rigaku D/Max-2550pc powder diffractometer equipped with Cu Kα radiation (λ = 1.54 Å). XPS measurements were conducted on a KRATOS AXIS ULTRA-DLD spectrometer with a monochromatic Al Kα radiation ($h\upsilon$ = 1486.6 eV). The morphologies of the products were observed by field-emission SEM on an FEI-sirion microscope and TEM on a JEM 2100F microscope. Raman spectra were collected on a Jobin-Yvon Labor Raman HR-800 Raman system using an Ar-ion laser of 514.5 nm at 10 mW. The carbon content analysis was conducted on a Flash EA 1112 tester.

Electrochemical Studies. The electrochemical Na-storage properties of the NiS/rGO were evaluated by charge/discharge cycling using CR2025-type coin cells. The electrode slurry was made by mixing 75 wt % active material (NiS/rGO, NiS, rGO), 15 wt % acetylene black, and 10 wt % polyvinylidene fluoride (PVDF) in *N*-methyl pyrrolidone (NMP) with magnetic stirring for 2 h. The working electrodes were made by coating the slurry onto Ni foam followed by drying at 100 °C under vacuum overnight. Coin-type half cells were assembled in an Ar-filled glovebox using Na foil as counterelectrode and Celgard 2300 polypropylene membrane as separator. The electrolyte was 1 M $NaClO_4$ dissolved in propylene carbonate (PC). The cells were charged and discharged at various current densities between 0.005 and 3 V vs Na/Na^+ on a Neware battery tester (Shenzhen, China). The specific capacity of NiS/rGO was calculated on the basis of the total weight of NiS and rGO. Electrochemical impedance spectroscopy (EIS) measurements were performed on a CHI660C electrochemistry workstation. The impedance plots were recorded by applying an ac voltage of 5 mV amplitude in the frequency range from 10 mHz to 100 kHz at charge (Na-extracted) states after the cells were cycled for 10 cycles and stayed at open circuit voltage for at least 10 h. All of the electrochemical measurements were carried out at room temperature.

RESULTS AND DISCUSSION

After the hydrothermal reaction, NiS tends to form rodlike structure with the diameter and length around 100 nm and 1 μm, respectively, as seen in Figure 1a. Clearly, a radial flowerlike morphology has been constructed by the aggregated NiS nanorods. High-resolution TEM (HRTEM) image and electron diffraction (ED) patterns indicate that the NiS nanorod exhibits a single-crystalline nature (Supporting Information (SI) Figure S1d). Interestingly, the radial flowerlike morphology cannot be observed with the addition of GO in the precursor (NiS/20rGO). Instead, a sheetlike morphology has formed as shown in Figure 1b. Intuitively, the sheetlike structure is constructed by sole rGO sheets. Nevertheless, the EDS mapping in Figure 1c undoubtedly indicates the presence of Ni and S, which is further confirmed to be NiS by XRD (SI, Figure S5a). This means that NiS also exhibits a sheetlike structure. The TEM image in Figure 1d reveals the sheetlike structure for both NiS and rGO, which makes it difficult to distinguish them from each other. It seems that the presence of GO or rGO can affect the crystallization process of NiS. Figure 1e shows the HRTEM image of NiS/20rGO, which exhibits a composite character with NiS nanosheets dispersed in rGO nanosheets. It should be noted that the NiS nanosheets are unstable and rapidly decompose into small-sized sheets (with well-defined lattice fringes) after electron beam irradiation, while the rGO sheets are relatively stable upon a short time of irradiation.

On the basis of the primary results, two possible mechanisms for the formation of NiS nanosheets are proposed: (i) NiS can grow into a sheetlike structure from the beginning since the oxygen-containing groups and/or defects on GO (or rGO) can serve as the nucleation/growth sites for NiS sheets, inhibiting them from growing into a rodlike structure; (ii) NiS initially crystallizes into rods in the early reaction stage, and then the rods recrystallize into sheets in the presence of GO (or rGO) as the reaction proceeds. In the latter case, GO (or rGO) can be considered as the "adhesive tape" to "pull" NiS nanosheets out of nanorods, similar to the process of preparing graphene by the "Scotch tape method".[1,30] Control experiments were conducted to clarify the formation mechanism of NiS sheets, where two hydrothermal reactions were performed using the pre-prepared bare NiS nanorods and rGO (SI, Figure S2) or NiS nanorods and GO (SI, Figure S3) as the precursors. The above reactions are referred to as ex situ hydrothermal reactions. The synthesis, characterization, and the related discussion of rGO and the ex situ products (NiS@20rGO-1, NiS@20rGO-2) are described in detail in the Experimental Section and Figures S1−S3 in the SI.

In both cases, the morphology of radially aggregated nanorods disappears after the ex situ hydrothermal reactions. Instead, typical morphologies of aggregated nanoparticles, aggregated nanosheets, and partially exfoliated nanorods emerge, which are verified to be NiS by EDS analysis (SI, Figure S4). Clearly, these morphologies are the intermediates between the pristine NiS nanorods and the nanosheets. Therefore, it can be concluded that GO (or rGO) can indeed induce the recrystallization of NiS from nanorods into nanosheets via a hydrothermal process. Considering the fact that the reduction of GO can be accomplished in a short time during the hydrothermal reaction (SI, Figure S5d), it is reasonable to infer that rGO plays a main role in inducing the recrystallization of NiS, namely, exfoliation of nanorods to nanosheets. Of note is that exfoliation of NiS rods is insufficient in both cases due likely to the inhomogeneous dispersion of NiS on rGO due to the large size of NiS nanorods and the restacking of the hydrophobic rGO sheets. To better understand the exfoliation mechanism, a series of NiS/rGO samples were prepared by the in situ hydrothermal reactions, where hydrosoluble $Ni(Ac)_2{\cdot}4H_2O$, thiourea, and GO were used as the precursors. It is expected that the electrostatic attraction between positively charged Ni^{2+} and negatively charged graphene oxide sheets[45] will favor the uniform dispersion of NiS nanorods on rGO sheets. The characterization of these in situ NiS/rGO samples is summarized in the SI in Figure S5.

dx.doi.org/10.1021/ic402948s | Inorg. Chem. 2014, 53, 3511−3518

Figure 2 shows the SEM images of in situ NiS/rGO products with different rGO contents. Unlike NiS/20rGO, NiS/rGO

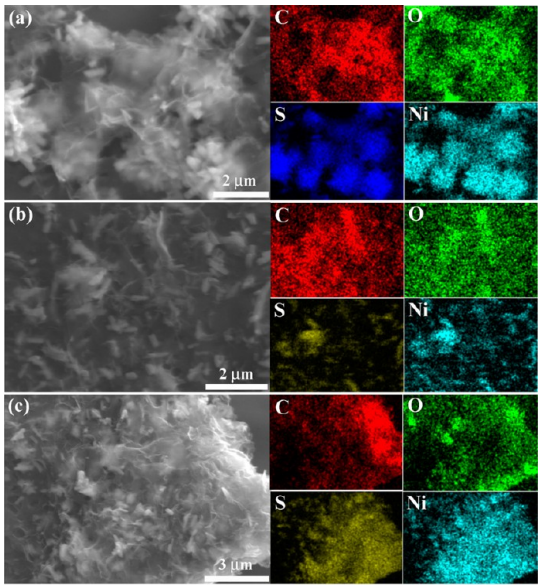

Figure 2. SEM images and EDS mapping of (a) NiS/5rGO, (b) NiS/10rGO, and (c) NiS/15rGO.

samples with lower rGO content exhibit insufficient exfoliation of NiS rods. As seen in Figure 2a, at a low rGO content (5 wt %), the aggregated rodlike morphology is still observable. These aggregates are surrounded by the thin sheets which are considered to be rGO sheets. EDS mapping for S and Ni indicates that the exfoliation of NiS rods should not be significant since the bright aggregates of S and Ni elements are clearly separated even though weak S and Ni signals are also present in between these bright aggregates. The presence of the weak S and Ni signals in between the bright aggregates, on the other hand, signifies the slight exfoliation of NiS nanorods, which occurs predominantly at the ends of the rods, where the contact with rGO is the most possible. TEM image of this sample (SI, Figure S6a) also reveals the presence of thin sheets at the ends of the rods and the obvious "etching" of the ends. At a higher rGO content (10 wt %), most of the aggregated rods are replaced by discrete nanorods as shown in Figure 2b. In addition, the length and diameter of the nanorods obviously decrease with the increased rGO content. The EDS mapping of S and Ni confirms that the discrete nanorods are NiS and that NiS sheets derived from NiS rods have "penetrated" into rGO as evidenced by the enhanced S or Ni signals in between these discrete NiS nanorods. The enhanced exfoliation of NiS nanorods with increased rGO content is further verified by TEM observation (SI, Figure S6b). When the rGO content is increased to 15 wt %, most of the rods have been converted into interconnected sheets due to an increased possibility for NiS to have contact with rGO (Figure 2c). EDS mapping demonstrates that S and Ni elements exhibit continuous and uniform distribution in rGO, indicating that NiS sheets are homogeneously dispersed in rGO sheets. As a result, the composite as a whole shows a sheetlike morphology. From the above experiments, we can conclude that the exfoliation of NiS rods is closely related to the presence of rGO.

Note that some short and thin rods can still be observed for NiS/15rGO although most of the rods have been transformed into sheets as mentioned above. This sample thus is an ideal choice for the investigation of the recrystallization process of NiS rods induced by rGO sheets. Four typical domains are selected for dark field TEM observation and EDS mapping (Figure 3). Figure 3a shows the TEM image and EDS mapping

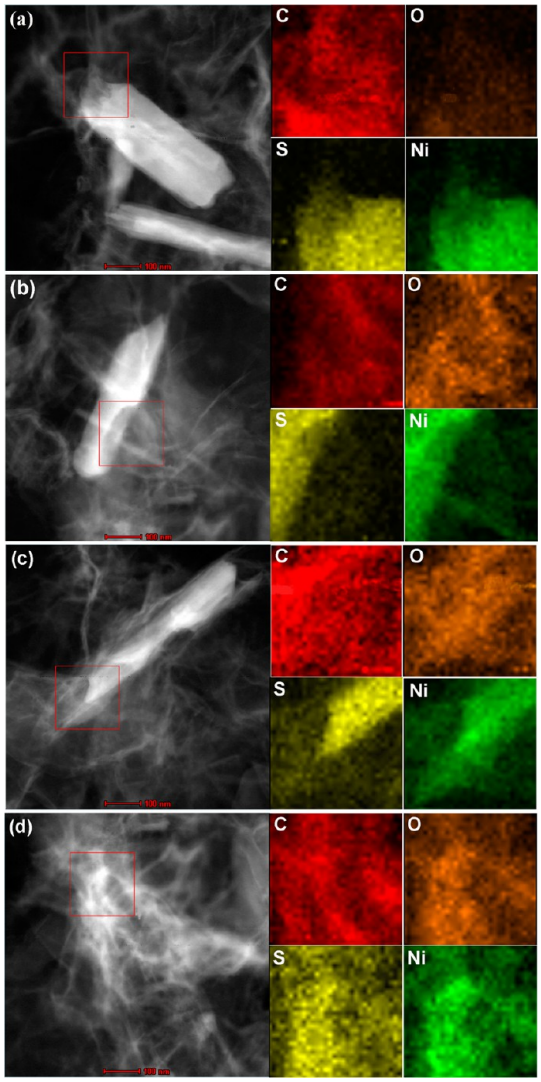

Figure 3. TEM images and EDS mapping of NiS/15rGO at different degrees of exfoliation of NiS nanorods.

in a domain surrounding the end of a rod. It is obvious that the exfoliation of the rod is proceeding, evidenced from the etched end. EDS mapping clearly reveals the presence of NiS in the entire selected domain, while the brightness contrast of S and Ni signals implies that NiS outside of the rod is exfoliated from the rod and has "penetrated" into the neighboring rGO sheets. This process can be vividly considered as a "dissolution" process of NiS in rGO due to the fact that NiS sheets are uniformly dispersing in rGO sheets and that this process is induced by rGO.

In Figure 3b, TEM and EDS mapping are performed on the side of a rod and its adjacent region. This domain is selected because obvious etching has occurred on the side of the rod. EDS mapping exhibits a clear brightness contrast of S and Ni signals, which fades out from the rod to the nearby area, indicative of the "dissolution" process of the NiS rod in rGO.

dx.doi.org/10.1021/ic402948s | Inorg. Chem. 2014, 53, 3511−3518

Figure 3c shows the TEM image of a NiS nanorod at its deep exfoliation stage, where the sheetlike matter is present all around the incomplete rod. EDS mapping in this domain also demonstrates the "dissolution" process of NiS in rGO. In the above three selected domains, strong C and O signals are all existing, suggesting that the "dissolution" or recrystallization of NiS rods is possibly induced by rGO and that the position at which NiS rod will "dissolve" or recrystallize is random as long as the contact with rGO has been established. Figure 3d gives the TEM image and EDS mapping in a domain where a NiS rod (or several rods) has been completely exfoliated into nanosheets. The uniform distribution of S, Ni, C, and O elements suggests that NiS nanosheets are distributed uniformly in rGO nanosheets, making the composite exhibit a sheetlike morphology as a whole. For NiS/15rGO, on one hand, we can still observe nearly complete NiS nanorods and aggregated NiS nanosheets (SI, Figure S7) because of the insufficient rGO content. The existence of these morphologies, on the other hand, proves our assumption that the NiS sheets are recrystallized from the NiS rods, rather than crystallized directly in the hydrothermal reaction.

To further clarify the exfoliation process of NiS nanorods, additional control experiments have been conducted by varying the reaction time (3−12 h), while keeping other conditions unchanged. Figure 4a shows the SEM image of the product

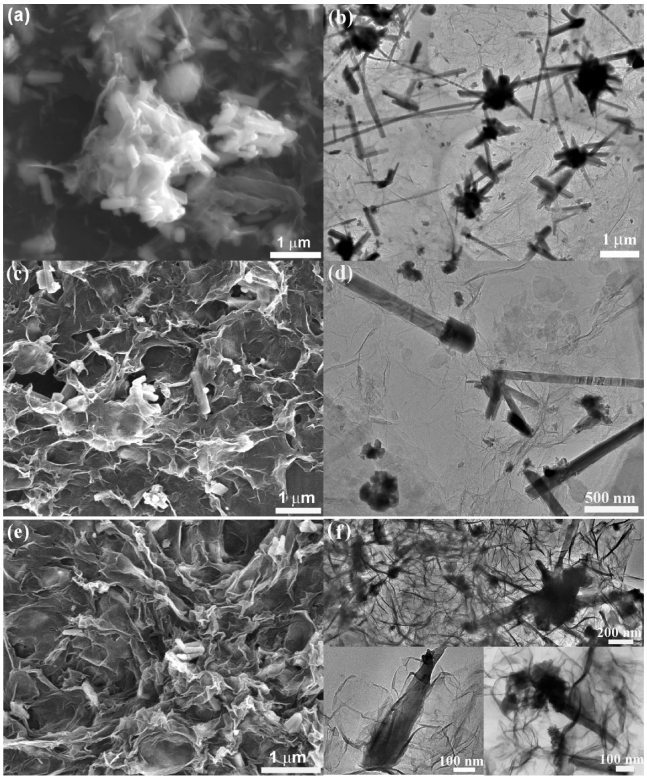

Figure 4. SEM and TEM images of NiS/20rGO after hydrothermal reactions for (a, b) 3 h, (c, d) 6 h, and (e, f) 12 h.

after 3 h hydrothermal reaction. Although the aggregates of NiS nanorods are still present, the length and thickness of the rods are obviously reduced, which is further confirmed by TEM observation (Figure 4b). Note that the rods aggregates are covered with thin sheets, which are considered to be rGO and NiS sheets. Some small aggregates and discrete etched rods are also observable, agreeing with the TEM result. The collapse of the large aggregates can be attributed to the function of rGO sheets. At a longer reaction time (6 h), large aggregates are rarely observed, and only small aggregates and discrete rods remain (Figure 4c). Furthermore, the lengths of the discrete rods and the rods in the small aggregates all show a remarkable decrease due to the enhanced exfoliation by rGO as shown in Figure 4d. In addition, the thickness of the rods is also decreasing as clearly revealed by TEM. Further increasing the reaction time (12 h) leads to the decrease in both number and size of rods aggregates and discrete rods (Figure 4e), indicating progressive exfoliation of NiS rods with the reaction time. Figure 4f gives the typical TEM images of this sample, which exhibits different exfoliation stages of NiS nanorods. On the basis of the above results, the exfoliation process of NiS nanorods is further clarified.

From the above analyses, some conclusions can be drawn: (1) NiS sheets are derived from the NiS rods by recrystallization, instead of crystallizing directly in the hydrothermal reaction via a nucleation/growth process; (2) the recrystallization process starts from the collapse of the large radial aggregates into smaller aggregates and further into discrete rods induced by rGO, during which the exfoliation of large aggregates, small aggregates, and discrete rods can occur simultaneously; (3) the position at which NiS rods will exfoliate is random, provided that rGO is present. Undoubtedly, rGO plays a critical role in recrystallizing NiS rods into sheets. A question, however, is still left open; that is, how is this realized? The educated guess is that the interaction between NiS and the oxygen-containing groups may underlie the exfoliation of NiS rods. The existence of residual oxygen-containing groups is verified by XPS (SI, Figure S5d) and EDS mapping (Figures 1−3), although significant deoxygenation does occur during the hydrothermal reactions (SI, Figure S5d). Previous work showed that residual oxygen-containing groups always exist in the chemically reduced graphene oxide even though reducing agent such as hydrazine hydrate[46] or sodium borohydride was used.[47] On the basis of the XPS analysis, the residual oxygen-containing groups in our rGO samples are mainly epoxy and/or hydroxyl groups, which are on the basal planes of rGO according to the Lerf−Klinowski model.[48] XPS analysis shows that the C/O atomic ratio in rGO is around 84:16 after the reduction reaction.

To prove the above assumption, S2p XPS was measured as presented in Figure 5. As seen in the figure, the spectrum can be deconvoluted into five peaks. The peaks at 161.5 and 162.5 eV indicate the presence of NiS, in agreement with the previous

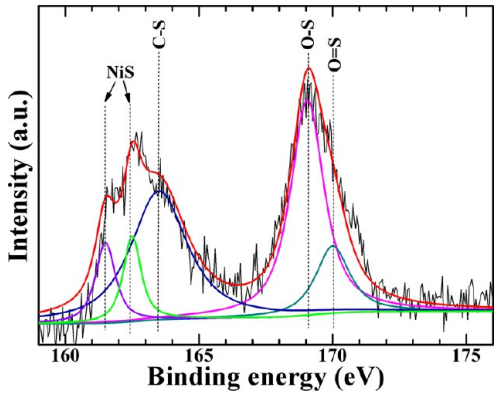

Figure 5. S2p XPS of NiS/20rGO.

dx.doi.org/10.1021/ic402948s | Inorg. Chem. 2014, 53, 3511−3518

report.[49] The peak at 163.5 eV denotes the formation of C−S bonds, while the construction of O−S bonds and O═S bonds can be identified by the peaks at 169 and 170 eV, respectively.[50] Apparently, in the above bonds, the −C−, −O−, and O═ configurations originate from rGO with residual oxygen-containing groups (C−C, C−O, C═O, and O−C═O, SI, Figure S5d), while the −S and ═S configurations come from NiS. Although the pristine NiS nanorods are well crystallized, the existence of some dangling or unsaturated bonds related to −S or ═S is highly possible on the surface layers of NiS. New chemical bonds (C−S, O−S, and O═S bonds) will form, provided that good contact has been established between surface dangling or unsaturated bonds on NiS and oxygen-containing groups on rGO. In addition, chemical bonding between Ni atoms and oxygen-containing groups should not be excluded.[51] The hydrothermal environment supplies the energy necessary for the construction of the new chemical bonds. Binding force between surface NiS layers and bulk NiS rods is thus weakened under the influence of the newly formed chemical bonds, while the energy provided by hydrothermal reaction promotes the peeling of the surface NiS layers from the rods eventually. Once the surface NiS layers have been exfoliated, new surface layers will naturally form with the construction of new angling or unsaturated bonds. Thus, continuous exfoliation will take place, given that there is sufficient rGO and that certain reaction conditions are supplied, which agrees with the experimental results that either insufficient rGO (Figures 2, 3) or inadequate reaction time (Figure 4) will result in incomplete recrystallization of NiS nanorods. The rGO induced recrystallization process of NiS nanorods is schematically illustrated in Figure 6.

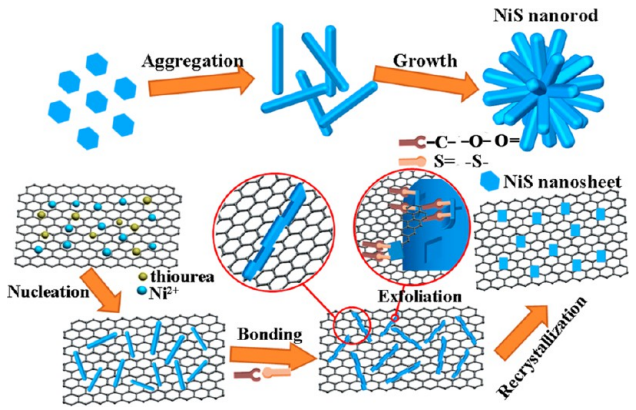

Figure 6. Schematic illustration of the exfoliation process and mechanism of NiS nanorods to nanosheets by rGO.

Figure 7a shows the charge and discharge curves of NiS/20rGO nanosheets and NiS nanorods at 50 mA g^{-1} for the first three cycles. The first charge (Na-extraction) and discharge (Na-insertion) capacities of NiS/20rGO are 524 and 701 mA h g^{-1}, while those of NiS are 349 and 513 mA h g^{-1}. Ex situ XRD was used to check the Na-extraction/insertion mechanism (SI, Figure S8). After discharge to 0.005 V, NiS peaks disappear with the appearance of Na_2S peaks. The weak and broad peaks of Na_2S suggest that Na_2S is poorly crystallized and/or is small in size. After charge to 3 V, the NiS peaks appear again, indicating that NiS lattices have recovered after charge. Thus, the reaction mechanism of NiS with Na is proposed as NiS + 2Na ↔ Na_2S + Ni. According the reaction, the theoretical capacity of NiS is 590 mA h g^{-1}, while that of NiS/20rGO is roughly estimated to be 496 mA h g^{-1} based on the theoretical capacity of NiS and the yieldable capacity of rGO (around 120 mA h g^{-1} for Na-extraction, SI, Figure S9). The higher capacity of NiS/20rGO can be attributed to the sheetlike structure and the conducting and dispersing effects of rGO that maximize the utilization of NiS. For both samples, the first irreversible capacity is due to the formation of solid electrolyte interface (SEI) film. Figure 7b compares the cycling stability between NiS/20rGO and NiS charged at 200 and 400 mA g^{-1} and discharged at 50 mA g^{-1}. The capacity of NiS/20rGO is calculated on the basis of the total weight of NiS and rGO. At a relatively large current density of 200 mA g^{-1}, NiS/20rGO can yield a capacity of 181 mA h g^{-1}. After 10 cycles, a charge capacity of 160 mA h g^{-1} is still obtainable. In contrast, although NiS nanorods can yield a similar initial charge capacity, it rapidly drops to 77 mA h g^{-1} after 10 cycles. A similar result is observed when the charge current density is increased to 400 mA g^{-1}. The better cycling stability can be attributed to the unique sheetlike structure of NiS that facilitates rapid Na-ion transport both at NiS/electrolyte interface and in bulk NiS. In addition, the interconnected rGO sheets construct a three-dimensional (3D) conducting network that not only enhances the electrode reaction kinetics but also buffers the volume changes during the Na-ion insertion/extraction process.

EIS was used to explain the different electrochemical behaviors between NiS/20rGO and NiS. As seen in Figure 7c, the Nyquist plots are composed of a depressed semicircle in the high-to-medium frequency region and a sloping line in the low-frequency region. The depressed semicircle consists of two partly overlapped semicircles. The plots are fitted by an equivalent circuit (inset in Figure 7c), where R_e denotes the electrolyte resistance, corresponding to the intercept of high-frequency semicircle at Z' axis. R_f and Q_1, corresponding to the high-frequency semicircle, represent the SEI layer resistance and dielectric relaxation capacitance, respectively. R_{ct} and Q_2, related to the middle-frequency semicircle, denote the charger transfer resistance and the associated double-layer capacitance, respectively, and Z_w is referred to as the Na-ion diffusion resistance in the bulk material.[52] The fitting results show that R_f and R_{ct} of NiS are 176 and 315 Ω, respectively, while those of NiS/20rGO are 182 and 71 Ω, respectively. The lower R_{ct} value of NiS/20rGO means more rapid electrochemical reaction kinetics at the electrode/electrolyte interface due to the improved electrical conductivity by rGO incorporation and unique sheetlike structure that facilitates Na-ion diffusion across the electrode/electrolyte interface.

CONCLUSIONS

In summary, the results of this work show that NiS nanorods can be recrystallized into nanosheets in the presence of rGO during the hydrothermal reaction. The recrystallization of NiS nanorods to nanosheets can be considered as a "dissolution" process of NiS rods in rGO sheets, considering the fact that NiS nanosheets are dispersed uniformly in rGOs nanosheets and that the exfoliation/dispersion process of NiS rods is induced by rGO sheets. The exfoliation process starts from the collapse of the radial rod aggregates into smaller aggregates and further into discrete rods, and the exfoliation of large aggregates, small aggregates, and discrete rods occurs simultaneously with the collapse of the large aggregates. The exfoliation can occur at any position on NiS rods, according to the presence of rGO.

dx.doi.org/10.1021/ic402948s | Inorg. Chem. 2014, 53, 3511−3518

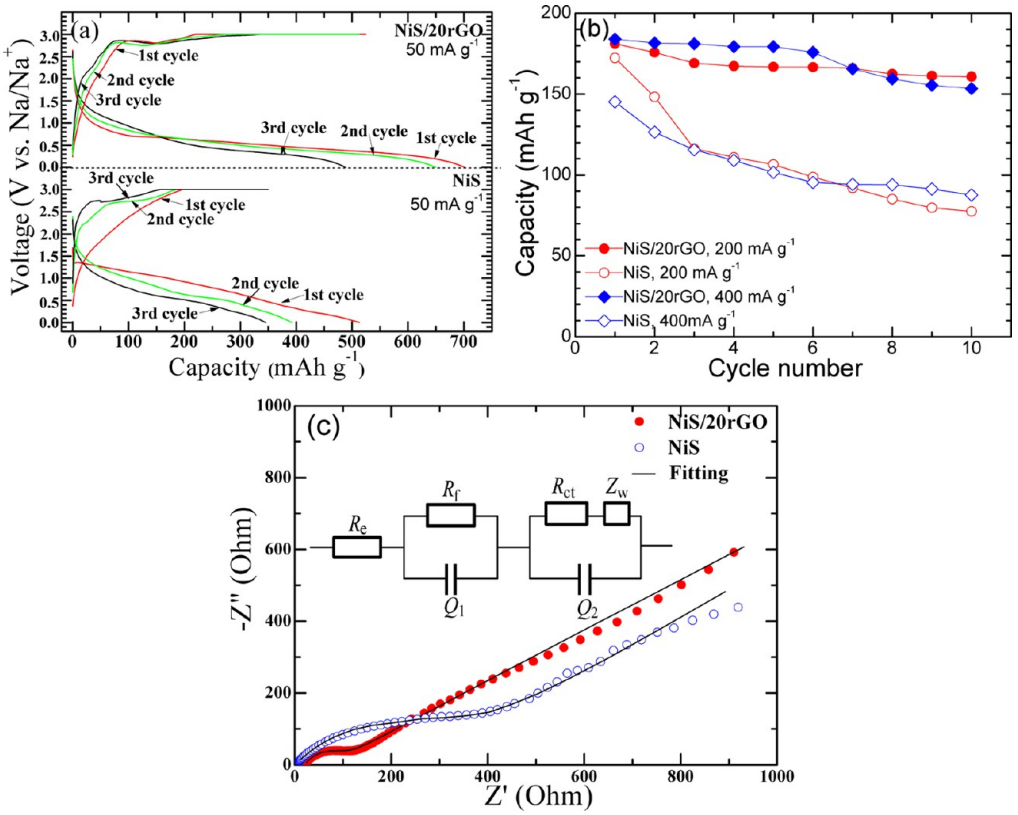

Figure 7. (a) Charge and discharge curves, (b) cycling stability and (b) EIS of NiS/20rGO and NiS nanorods.

The hydrothermal reaction promotes chemical bonding between surface dangling or unsaturated bonds on NiS rods and oxygen-containing groups on rGO sheets, which weakens the binding force between surface NiS layers and bulk NiS rods, As a result, the surface NiS layers will be "pulled" out of the rods by the new chemical bonds under the hydrothermal environment. NiS/20rGO nanosheets show better electrochemical properties than NiS nanorods due to the unique sheetlike structure of NiS in NiS/20rGO and the introduction of rGO that not only provides a 3D conducting network but also buffers the volume changes of NiS upon repeated cycling.

■ ASSOCIATED CONTENT

Supporting Information

XRD patterns GO and rGO, TEM images of rGO, HRTEM of an individual NiS nanorod, SEM images of NiS@20rGO-1 and NiS@20rGO-2, EDS mapping of NiS@20rGO-2, XRD patterns of NiS and NiS/rGO composites, Raman spectra of GO and NiS/20rGO, XPS survey of NiS/20rGO, C1s XPS of NiS/20rGO, GO, and rGO (1 h reaction), Ni2p XPS of NiS before and after the hydrothermal process, TEM images of NiS/5rGO and NiS/10rGO, SEM images and EDS mapping of NiS/15rGO, the first three charge and discharge curves of rGO at 50 mA g^{-1}, and the ex situ XRD of NiS during discharge and charge. This material is available free of charge via the Internet at http://pubs.acs.org.

■ AUTHOR INFORMATION

Corresponding Authors

*Tel./Fax: +86-571-87951451. E-mail: xiejian1977@zju.edu.cn.
*E-mail: zhaoxb@zju.edu.cn.

Notes

The authors declare no competing financial interest.

■ ACKNOWLEDGMENTS

This work was supported by the National Basic Research Program of China (2013CB934001), the National Natural Science Foundation of China (No. 51101139), the Qianjiang Talents Project of Science Technology Department of Zhejiang Province (2011R10021), Key Science and Technology Innovation Team of Zhejiang Province under Grant Number 2010R50013, and Program for Innovative Research Team in University of Ministry of Education of China (IRT13037).

■ REFERENCES

(1) Novoselov, K. S.; Geim, A. K.; Morozov, S. V.; Jiang, D.; Zhang, Y.; Dubonos, S. V.; Grigorieva, I. V.; Firsov, A. A. *Science* **2004**, *306*, 666−669.
(2) Stoller, M. D.; Park, S.; Zhu, Y. W.; An, J. H.; Ruoff, R. S. *Nano Lett.* **2008**, *8*, 3498−3502.
(3) Park, S.; An, J. H.; Jung, I. W.; Piner, R. D.; An, S. J.; Li, X. S.; Velamakanni, A.; Ruoff, R. S. *Nano Lett.* **2009**, *9*, 1593−1597.
(4) Du, X.; Skachko, I.; Barker, A.; Andrei, E. Y. *Nat. Nanotechnol.* **2008**, *3*, 491−495.
(5) Chen, H. Q.; Müller, M. B.; Gilmore, K. J.; Wallace, G. G.; Li., D. *Adv. Mater.* **2008**, *20*, 3557−3561.
(6) Dutta, S.; Pati, S. K. *J. Mater. Chem.* **2010**, *20*, 8207−8223.
(7) Zhu, Y. W.; Murali, S.; Cai, W. W.; Li, X. S.; Suk, J. W.; Potts, J. R.; Ruoff, R. S. *Adv. Mater.* **2010**, *22*, 3906−3924.
(8) Wei, D. C.; Liu, Y. Q. *Adv. Mater.* **2010**, *22*, 3225−3241.
(9) Huang, X.; Yin, Z. Y.; Wu, S. X.; Qi, X. Y.; He, Q. Y.; Zhang, Q. C.; Yan, Q. Y.; Boey, F.; Zhang, H. *Small* **2011**, *7*, 1876−1902.
(10) Sun, Y. Q.; Wu, Q.; Shi, G. Q. *Energy Environ. Sci.* **2011**, *4*, 1113−1132.
(11) Guo, S. J.; Dong, S. J. *Chem. Soc. Rev.* **2011**, *40*, 2644−2672.

dx.doi.org/10.1021/ic402948s | *Inorg. Chem.* 2014, 53, 3511−3518

(12) Zhang, N.; Zhang, Y. H.; Xu, Y. J. *Nanoscale* **2012**, *4*, 5792−5813.
(13) Liu, J.; Xue, Y. H.; Zhang, M.; Dai, L. M. *MRS Bull.* **2012**, *37*, 1265−1272.
(14) Zhu, C. Z.; Dong, S. J. *Nanoscale* **2013**, *5*, 1753−1767.
(15) Rao, C. N. R.; Ramakrishna Matte, H. S. S.; Subrahmanyam, K. S. *Acc. Chem. Res.* **2013**, *46*, 149−159.
(16) Xu, M. S.; Liang, T.; Shi, M. M.; Chen, H. Z. *Chem. Rev.* **2013**, *113*, 3766−3798.
(17) Li, H.; Yin, Z. Y.; He, Q. Y.; Li, H.; Huang, X.; Lu, G.; Fam, D. W. H.; Tok, A. I. Y.; Zhang, Q.; Zhang, H. *Small* **2012**, *8*, 63−67.
(18) Radisavljevic, B.; Radenovic, A.; Brivio, J.; Giacometti, V.; Kis, A. *Nat. Nanotechnol.* **2011**, *6*, 147−150.
(19) Wu, S. X.; Zeng, Z. Y.; He, Q. Y.; Wang, Z. J.; Wang, S. J.; Du, Y. P.; Yin, Z. Y.; Sun, X. P.; Chen, W.; Zhang, H. *Small* **2012**, *8*, 2264−2270.
(20) Golberg, D.; Bando, Y.; Huang, Y.; Terao, T.; Mitome, M.; Tang, C. C.; Zhi, C. Y. *ACS Nano* **2010**, *4*, 2979−2993.
(21) Rao, C. N. R.; Nag, A. *Eur. J. Inorg. Chem.* **2010**, 4244−4250.
(22) Hwang, H.; Kim, H.; Cho, J. *Nano Lett.* **2011**, *11*, 4826−4830.
(23) Bhandavat, R.; David, L.; Singh, G. *J. Phys. Chem. Lett.* **2012**, *3*, 1523−1530.
(24) Liu, J. H.; Liu, X. W. *Adv. Mater.* **2012**, *24*, 4097−4111.
(25) Coleman, J. N.; Lotya, M.; O'Neill, A.; Bergin, S. D.; King, P. J.; Khan, U.; Young, K.; Gaucher, A.; De, S.; Smith, R. J.; Shvets, I. V.; Arora, S. K.; Stanton, G.; Kim, H. Y.; Lee, K.; Kim, G. T.; Duesberg, G. S.; Hallam, T.; Boland, J. J.; Wang, J. J.; Donegan, J. F.; Grunlan, J. C.; Moriarty, G.; Shmeliov, A.; Nicholls, R. J.; Perkins, J. M.; Grieveson, E. M.; Theuwissen, K.; McComb, D. W.; Nellist, P. D.; Nicolosi, V. *Science* **2011**, *331*, 568−571.
(26) Nicolosi, V.; Chhowalla, M.; Kanatzidis, M. G.; Strano, M. S.; Coleman, J. N. *Science* **2013**, *340*, 1226419.
(27) Song, L.; Ci, L. J.; Lu, H.; Sorokin, P. B.; Jin, C. H.; Ni, J.; Kvashnin, A. G.; Kvashnin, D. G.; Lou, J.; Yakobson, B. I.; Ajayan, P. M. *Nano Lett.* **2010**, *10*, 3209−3215.
(28) Schliehe, C.; Juarez, B. H.; Pelletier, M.; Jander, S.; Greshnykh, D.; Nagel, M.; Meyer, A.; Foerster, S.; Kornowski, A.; Klinke, C.; Weller, H. *Science* **2010**, *329*, 550−553.
(29) Xu, C.; Zeng, Y.; Rui, X. H.; Xiao, N.; Zhu, J. X.; Zhang, W. Y.; Chen, J.; Liu, W. L.; Tan, H. T.; Hng, H. H.; Yan, Q. Y. *ACS Nano* **2012**, *6*, 4713−4721.
(30) Novoselov, K. S.; Jiang, D.; Schedin, F.; Booth, T. J.; Khotkevich, V. V.; Morozov, S. V.; Geim, A. K. *Proc. Natl. Acad. Sci.U.S.A.* **2005**, *102*, 10451−10453.
(31) Paredes, J. I.; Villar Rodil, S.; Martínez Alonso, A.; Tascón, J. M. D. *Langmuir* **2008**, *24*, 10560−10564.
(32) Dreyer, D. R.; Park, S.; Bielawski, C. W.; Ruoff, R. S. *Chem. Soc. Rev.* **2010**, *39*, 228−240.
(33) Mao, S.; Pu, H. H.; Chen, J. H. *RSC Adv.* **2012**, *2*, 2643−2662.
(34) Lerf, A.; He, H. Y.; Riedl, T.; Forster, M.; Klinowski, J. *Solid State Ionics* **1997**, *101*−*103*, 857−862.
(35) Loh, K. P.; Bao, Q. L.; Ang, P. K.; Yang, J. X. *J. Mater. Chem.* **2010**, *20*, 2277−2289.
(36) Chen, D.; Feng, H. B.; Li, J. H. *Chem. Rev.* **2012**, *112*, 6027−6053.
(37) Georgakilas, V.; Otyepka, M.; Bourlinos, A. B.; Chandra, V.; Kim, N.; Christian Kemp, K.; Hobza, P.; Zboril, R.; Kim, K. S. *Chem. Rev.* **2012**, *112*, 6156−6214.
(38) Wang, H. L.; Dai, H. J. *Chem. Soc. Rev.* **2013**, *42*, 3088−3113.
(39) Li, N.; Cao, M. H.; Hu, C. W. *Nanoscale* **2012**, *4*, 6205−6218.
(40) Palomares, V.; Serras, P.; Villaluenga, I.; Hueso, K. B.; Carretero Gonźalez, J.; Rojo, T. *Energy Environ. Sci.* **2012**, *5*, 5884−5901.
(41) Kim, S. W.; Seo, D. H.; Ma, X. H.; Ceder, G.; Kang, K. *Adv. Energy Mater.* **2012**, *2*, 710−721.
(42) Slater, M. D.; Kim, D.; Lee, E.; Johnson, C. S. *Adv. Funct. Mater.* **2013**, *23*, 947−958.
(43) Doeff, M. M.; Ma, Y. P.; Visco, S. J.; De Jonghe, L. C. *J. Electrochem. Soc.* **1993**, *140*, L169−L170.
(44) Hummers, W. S.; Offeman, R. E. *J. Am. Chem. Soc.* **1958**, *80*, 1339−1339.
(45) Li, D.; Müller, M. B.; Gilje, S.; Kaner, R. B.; Wallace, G. G. *Nat. Nanotechnol.* **2008**, *3*, 101−105.
(46) Stankovich, S.; Dikin, D. A.; Piner, R. D.; Kohlhaas, K. A.; Kleinhammes, A.; Jia, Y. Y.; Wu, Y.; Nguyen, S. T.; Ruoff, R. S. *Carbon* **2007**, *45*, 1558−1565.
(47) Shi, H. J.; Kim, K. K.; Benayad, A.; Yoon, S. M.; Park, H. K.; Jung, I. S.; Jin, M. H.; Jeong, H. K.; Kim, J. M.; Choi, J. Y.; Lee, Y. H. *Adv. Funct. Mater.* **2009**, *19*, 1987−1992.
(48) Lerf, A.; He, H. Y.; Forster, M.; Klinowski, J. *J. Phys. Chem. B* **1998**, *102*, 4477−4482.
(49) Goh, W.; Buckley, A. N.; Lamb, R. N.; Skinner, W. M.; Pring, A.; Wang, H.; Fan, L. J.; Jang, L. Y.; Lai, L. J.; Yang, Y. W. *Phys. Chem. Miner.* **2006**, *33*, 98−105.
(50) Lindberg, B. J.; Hamrin, K.; Johansson, G.; Gelius, U.; Fahlman, A.; Nordling, C.; Siegbahn, K. *Phys. Scr.* **1970**, *1*, 286−298.
(51) Zhou, G. M.; Wang, D. W.; Yin, L. C.; Li, N.; Li, F.; Cheng, H. M. *ACS Nano* **2012**, *6*, 3214−3223.
(52) Aurbach, D. *J. Power Sources* **2000**, *89*, 206−218.